

SELF-HEALING EFFECTS OF COPPER ON 3-D PRINTED 420 STAINLESS STEEL

By

Zhenyu Chen

A THESIS

Submitted to
Michigan State University
in partial fulfillment of the requirements
for the degree of

Mechanical Engineering-Master of Science

2018

ABSTRACT

SELF-HEALING EFFECTS OF COPPER ON 3-D PRINTED 420 STAINLESS STEEL

By

Zhenyu Chen

The purpose of this thesis is to investigate the possibility of attaining the self-healing property in metallic alloys produced by the 3D printing technology. Stainless steel (SS) is used as our metal system and the copper element is added to improve the self-healing property. The sintering additive of 0.5% of boron was found to improve the final density dramatically and reduce the sintering temperature, enabling us to improve the mechanical properties. This boron additive was used to print the Fe-Cu alloys. After the printing procedure, the samples are then cut into a dog-bone shaped tensile sample whose surfaces are polished before the fatigue test. During the fatigue test, we recorded the stress-number of cycle (S-N) diagram. Knowing the limit of the S-N diagram, specimens were taken to the fatigue cycle near the limit to produce minor damages/cracks. After that, the healing process of heating the specimen is applied to improve in their fatigue behavior. With the addition of 3% of Cu element, the self-healing property of steel can be enhanced dramatically. Under 407 MPa of stress, the sample without the inclusion of Cu breaks after 79019+76274 cycles, where the first number means the preloading cycles while the second one indicates the life cycles until it breaks after the heat treatment. While the performance of the sample with 3% of Cu can reach to 86893+118147 circles under 419 MPa of stress. The self-healing mechanism of Fe-Cu alloys comes from that the copper atoms can diffuse into the iron matrix to heal the microscopic cracks, which enable us to achieve “self-healing”.

ACKNOWLEDGEMENTS

I would like to express my appreciation to my advisor, Dr. Patrick Kwon. Thank you for giving me this opportunity to join your 3-D printing group, having a chance to learn the most advanced and potential technologies and instructing me patiently through all my master study. Also, all the materials and mechanical processes in my study costs lots of resources. I am so grateful that you give me all of supports to help me finish this study.

Thanks to everyone in our 3-D printing group for teaching the basic knowledge about 3-D printing processes when I get into the technology for the first time and introducing all machines and how to operate them step by step. Specially, thanks to Dr. Truong Do. Whenever I need help or have questions about anything in this research, he helped me a lot and supported me. In fact, his previous study provided the foundation to do my research.

Thanks to KITECH, in Korea, for helping me cut the samples by WEDM and doing the fatigue test for me.

TABLE OF CONTENTS

LIST OF TABLES	vi
LIST OF FIGURES	vii
KEY TO ABBREVIATIONS	viii
Chapter 1 INTRODUCTION	1
1.1 Motivation	1
1.2 Background	3
1.2.1 Introduction of 3D printing technologies	3
1.2.2 Self-healing materials	6
1.2.3 Self-healing Effects in Fe-based alloys	9
1.2.4 Materials preparation	10
1.2.5 Properties of copper-iron alloy	13
1.2.6 Boron-additives effects on 420 stainless steel	15
Chapter 2 RESEARCH OBJECTIVES	16
Chapter 3 EXPERIMENT PROCESSES	18
3.1 Samples preparation	18
3.1.1 Powder additive amount	18
3.1.2 Printing	21
3.1.3 Curing	21
3.1.4 Sintering	21
3.1.5 Shapes and density test	22
3.2 Specimens preparation and processes of fatigue test	27
3.2.1 Specimens printing	27
3.2.2 Grinding	28
3.2.3 Surface finish processing	28
3.2.4 WEDM	29
3.2.5 Fatigue test	30
3.2.6 Heat treatment	31
Chapter 4 RESULT DISSCUSION AND ANALYSIS	33
4.1 S-N diagram	33
4.1.1 UTS testing	33

4.1.2 Stress and life cycle for healable samples	34
4.1.3 Stress and life cycle for standard samples	38
4.2 Result of improvement of fatigue life after healing.....	42
4.3 SEM images	43
Chapter 5 CONCLUSIONS	46
5.1 Difficulties and problems.....	46
5.2 Data analysis and conclusions	46
BIBLIOGRAPHY	49

LIST OF TABLES

Table 1: six experiments with different additives in different sintering temperature to obtain full dense samples.....	18
Table 2: density of additives used in this research	24
Table 3: the density and relative density of six experiments which are to obtain full dense sample.....	24
Table 4: UTS test result for sample with copper and without copper.....	33
Table 5: stress and life cycle for samples with copper	34
Table 6: life cycle of samples with copper at 450 and 380 MPa.....	36
Table 7: life cycle of samples with copper at 450 and 380 MPa for red linear trend line.....	37
Table 8: stress and life cycle for samples without copper.....	38
Table 9: life cycle of samples without copper at 450 and 380 MPa	39
Table 10: life cycle of samples without copper at 450 and 380 MPa for linear line	39
Table 11: life cycles of both types of samples before and after heat treatment to reflect the improvement on fatigue behavior.....	42

LIST OF FIGURES

Figure 1. An example of complicated metal sample. Figure from Ref [3]	1
Figure 2. Schematic diagram of a 3D printer. Figure from Ref [6]	5
Figure 3. The healing mechanism incorporating encapsulated healing phase and embedded catalyst particles in a polymer matrix. Figure from Ref [25].	8
Figure 4. the relationship between Atomic percent and weight percent of copper in iron-copper alloy and temperature	11
Figure 5. the relationship between mass fraction of copper in iron-copper alloy and temperature	12
Figure 6. cubic samples after sintering under 1150°C for 6 hours	27
Figure 7. the dimension of samples with dog-bond shape for fatigue test	29
Figure 8. A broken sample after fatigue test	31
Figure 9. S-N diagram for samples with copper (healable sample)	35
Figure 10. S-N diagram for samples without copper (standard sample)	40
Figure 11. S-N diagram for healable sample and standard sample	41
Figure 12. image of grain boundaries of samples without copper	43
Figure 13. image of grain boundaries of samples with copper	43
Figure 14. percentage of all elements in random spot picked in SEM image	44
Figure 15. the distribution of all elements in the spot picked	45

KEY TO ABBREVIATIONS

3DP	Three-Dimension Printing
WEDM	Wire Electrical Discharge Machining
ASTM	American Society for Testing and Materials
FDM	Fused Deposition Modeling
SLS	Selective Laser Sintering
LOM	Laminated Object Manufacturing
BJ	Binder Jetting
LENS	Laser Engineered Net Shaping
SLA	Stereo Lithography Apparatus
P/M	Powder Metallurgy
UTS	Ultimate Tensile Strength
CNC	Computer Numerical Control
SEM	Scanning Electron Microscope
FDM	Fused Deposition Modeling
CAM	Computer-Aided Manufacturing
CAD	Computer-Aided Design
SS	Stainless Steel

Chapter 1 INTRODUCTION

1.1 Motivation

Traditionally, the metal-based materials are initially started with one form of casting methods, which requires to heat the metal to liquid state and inject the metal liquid into the well-shaped mold to form desired shapes. Although the traditional casting method has been widely used, it has its intrinsic weaknesses [1,2] which are

1) The casting method requires to predesign the mold, which is very complicated and expensive. The use of mold also limits the casting method to be applied to simple shapes. For complicate shaped parts, neither the cast method can be used nor it will be very difficult to fabricate the mold. For example, the device shown in Fig. 1 is not possible to be processed by the traditional casting method due to its complexity.



Figure 1. An example of complicated metal sample. Figure from Ref [3]

2) Defects are unavoidable. The traditional casting method relies on the feasible flow or motion of metal liquid into a mold. As a result, the viscosity of the molten metal liquid can affect the quality of the casted samples. Usually, typical defects such as air bubbles are easily formed in the casted parts in the area where metal liquid cannot fill quickly.

3) In designing new parts, the casting method is very expensive due to the construction of molds that can produce desired parts. In a new design, one cannot guarantee the success of a single design. As a result, one may need to design multiple molds, which can be extremely expensive.

In metal 3D printing, usually the powder is used to print parts. The advantage of the powder is that additional powder with distinct compositions and weight fraction can be premixed before printing to improve mechanical properties. In printing, powder is bonded together by the binder phase in a layer by layer approach. However, the main advantage of 3D printing is design freedom, that is the ability to produce any complex geometries including interior geometry without the need for tooling. Even in this scenario, the main disadvantage of 3D printing is the deficiency in the strength and density of the final part compared to, for example, the forged parts without any reasonable method to induce strain hardening to the printed part. In this research, we dedicate to improve the mechanical strengths of stainless steel (SS) parts. Small amounts of copper and boron are added to improve the mechanical strengths, where boron helps enhancing sintering for improved density and copper improves the fatigue strength by providing self-healing property. If so, we have contributed by reducing the overall cost of manufacturing, improved the mechanical properties of the final parts produced by 3D printing.

1.2 Background

1.2.1 Introduction of 3D printing technologies

3D printing, also referred to as additive manufacturing (AM), which is a method of basically synthesizing a three-dimensional object directly from the model created by computer aided design (CAD) package. AM is formally defined by American Society for Testing and Materials (ASTM) Committee F42 as *“a process of joining materials to make objects from 3D model data, usually layer upon layer, as opposed to subtractive manufacturing methodologies”*, and 3D printing is defined as *“the fabrication of objects through the deposition of a material using a print head, nozzle, or another printer technology, often used synonymously with additive manufacturing”* [4]. Additive manufacturing just as its name implies that an object is built by adding layers successively from the base to fabricate parts. Various technologies were developed, including Fused Deposition Modeling (FDM), Selective Laser Sintering (SLS), Laminated Object Manufacturing (LOM), Binder Jetting Printing (BJP), Laser Engineered Net Shaping (LENS), and Stereo Lithography Apparatus (SLA) [5, 6]. In BJP, a binder phase is applied onto a layer of powder and by repeating the process in a layer by layer fashion and the 3D shape of a part can be attained. The 3D objects can be converted directly from 3D models with any shapes and geometries.

The origin of a 3-D printer can be traced as far back as the end of 19 century. In European and American countries, commodity economy was developed rapidly due to the industrial revolutions. Transformation of production technology became a popular theme at that time. Rapid prototyping technology began sprouting for satisfying the requirements of research and product design. In 1892,

Blanter proposed to make topographic map layer by layer for the first time [42]. In 1981, a Japanese researcher, Hideo Kodama from Nagoya Municipal Industrial Research Institute, invented two AM fabricating methods to build up the first solid plastic model, where the UV light exposure area was controlled by a mask pattern or the scanning fiber transmitter [44]. In 1984, Charles Hull designed a new solid image technology called Stereo lithography (STL), applied in rapid prototyping area [43, 44]. He also developed famous STL format, which became industrial standard of CAD/CAM file format. In 1992, a company called Stratasys created the first 3-D printer based on FDM technology-3D Modeler, which represented that FDM technology stepped to the stage of commercial application. In 1993, Professor Emanuel Sachs invented Three-Dimension (3-D) Printing technology to build up models by combining metal powder or ceramics powder layer by layer via binder [45]. Now many companies are building their own 3-D printers for various materials and applications. In 2005, Z corporation invented the first high precision color 3-D printer in the world [46].

In most of these systems, a printed part is typically built accumulatively layer upon layer, using plastic filament or metal wire unwound from a coil. Figure 2 illustrates a schematic counterpart of a 3D printer. The motion mechanism used is often an X-Y-Z rectilinear design, resembling 3-axis CNC machine tools, although other mechanical designs such as delta robot 3D printers are also available [6].

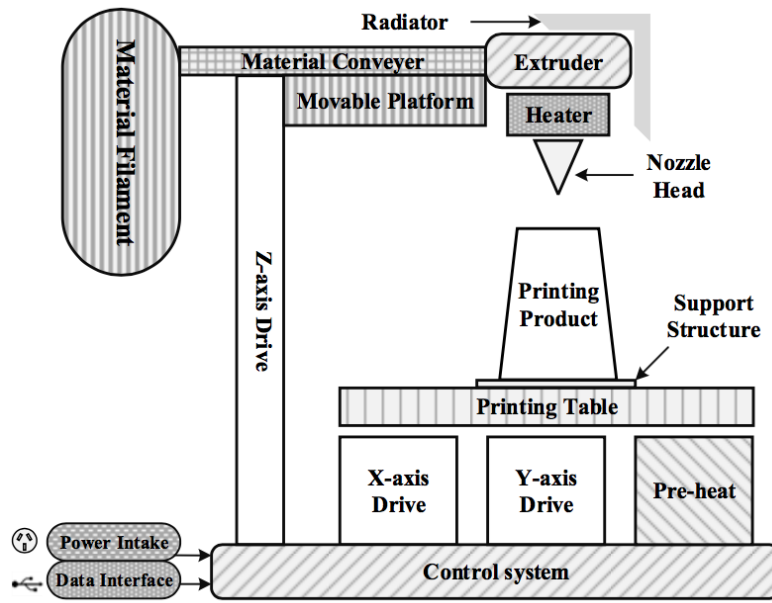


Figure 2. Schematic diagram of a 3D printer. Figure from Ref [6]

After many years of developments, the 3-D printing technology has been widely applied in many fields due to its advantages [3, 7-9] from manufacturing to medicine and from architecture to custom art and design. For examples, many concept car models are made with rapid prototyping robots [47]. Nike uses 3-D printing to manufacture Vapor Laser Talon football shoes for Athletes [48]. Also, 3-D printing is applied to produce some mechanical parts for cars and aircrafts [49]. Additionally, clothes, food, medications and artistic works are 3-D printed for various purposes [50].

Compared to the cast method, 3-D printing possesses many advantages [10-12]: First, based on the design with CAD, 3D printing allows to fabricate complicated samples without expensive molds. Second, with 3D printing, the ideas of new products can be developed quicker. The

development cycle from an initial design concept to a prototype/physical part can be substantially shrunk from what might have been months to a matter of days. Third, manufacturing equipment requires expensive investments. 3D printing allows a product developer to make breakthroughs at early stages relatively inexpensively eventually leading to better products.

1.2.2 Self-healing materials

Creep, a well-known phenomenon, is often regarded as an undesired effect that may limit the lifetime of (critical) steel components. It may lead to premature fracture below the static yield strength when exposed to elevated temperatures for an extended period of time under a constant applied stress. This type of failure results from the formation, growth and coalescence of nanoscale cavities and cracks [13]. For centuries, people have made continuous efforts to improve the structural properties of engineering materials in order to prevent damages. Manufacturing processes are optimized to minimize the formation of cracks and other defects at the initial stage. However, the growth and coalescence of the ultra-fine cracks and cavities in the following stages can lead to the fracture of materials. Therefore, it is important to periodically inspect structural components and repair critical damage. This is generally time consuming and expensive. It was recently recognized that the formation of damage is not problematic as long as the damage can be healed by the material itself. So self-healing materials are quite attractive for applications where reliability and durability are essential [14-16]. Self-healing materials are inspired by the natural processes such as blood clot and healing of broken bones. In biological systems, a cut on a finger can spontaneously stop bleeding while the new skin is formed under the clot and a tree can be also

healed its damage to its trunk or branches by itself. In the last decade, numerous researches work on self-healing materials have led to the development of several types of man-made materials, i.e. polymers [17-19], ceramics [20, 21] and concrete [14, 22, 23].

Although different materials have their own self-healing mechanism, there are some fundamental principles to design a potential self-healing material. Fig. 3 illustrates one example of the self-healing process [24]. The existence of a mobile phase is the pre-requisite self-healing for a self-healing material. One (or more) component in the material has to be mobile with a driving force towards the damage sites. The mobile phase can be moved to the crack regions and put the two surfaces together, thereby acting as a healing agent and partially or completely repairing the damage. The mobile agent finally stops the crack moving further, which results in partially or fully restored mechanical properties.

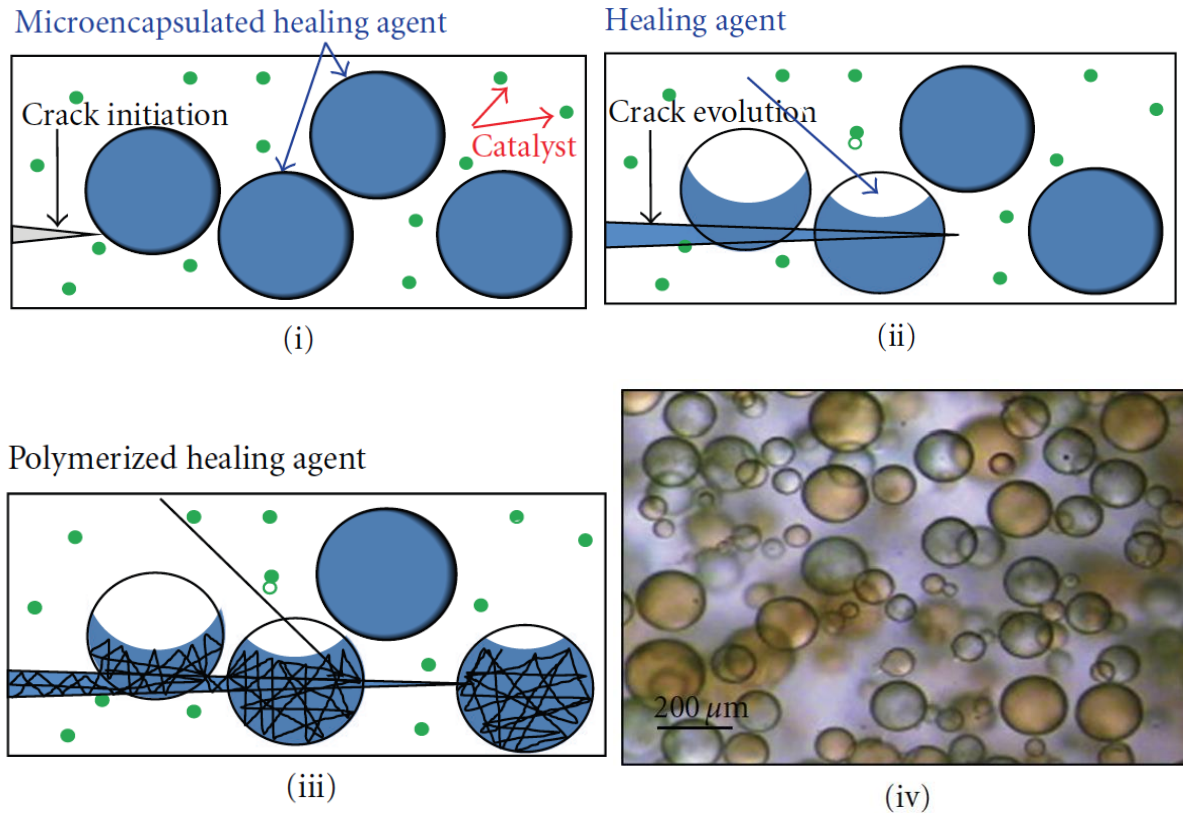


Figure 3. The healing mechanism incorporating encapsulated healing phase and embedded catalyst particles in a polymer matrix. Figure from Ref [25].

Figure 3 contains four phenomenon that has to occur to induce the self-healing: (i) the formation of cracks in the matrix; (ii) crack ruptures the microcapsules, releasing liquid healing phase into crack region; (iii) healing phase polymerizing upon contact with catalyst, connecting and closing the cracks; (iv) a typical SEM image of the urea-formaldehyde microcapsules containing dicyclopentadiene prepared by emulsion in situ microencapsulation [25].

The self healing phenomenon has also been studied in many metal systems [26]. For example, Laha et al. [15, 16] studied the effect of B segregation and Cu-containing 18Cr-12Ni-Nb on the

self healing property of austenitic stainless steel. The boron nitride precipitation effect on the creep cavitation in austenitic SS was investigated by Shinya et al. [27]. Except the use of single element to improve the self healing property, the combination of copper, boron and cerium have been used in type 347 austenitic steel to improve creep rupture strength [19]. Apart from steels, the self healing properties in Al-based shape memory alloys have also been widely studied. This includes the systems AlSi[28], Al+NiTi [29], commercial ZnAlCu [30], and Al+Al₂O₃+SnPb [31] etc.

1.2.3 Self-healing Effects in Fe-based alloys

Due to its tunable mechanical properties which make it possible to get an optimised combination of strength and ductility, steel is a popular construction material in many fields. However, under specific stress range and at relatively high temperatures, due to the formation, growth and coalescence of nanoscale cracks, steel exhibits premature and low-ductility creep fracture. Most high-strength high-temperature steels demonstrate creep cavity-induced creep fracture at their long-term high-temperature services. Self-healing is a promising new approach to elongate the service life of steel components, for example, in gas turbines and power plants, which operate at high temperatures [14].

Recently, Leha et al. [15-17,19] have found that creep damage can be healed in heat-resistant steels. The cavity growth rate can be decreased and the creep life can be improved with the addition of boron, copper, nitrogen and boron to the titanium (321BCe) and niobium-(347BCe)-containing steels [16]. The dynamic precipitation of BN and Cu segregation on cavity surfaces is the key

factor to improve the creep properties. In some other works, copper precipitation was also observed at the crack regions in Fe-Cu-B-N and Fe-Cu alloys [20-21, 32]. However, besides the copper precipitates, small spherical Cu precipitates have also been found in the matrix, which increases the self-healing characteristics. The reason is that smaller copper particles are able to diffuse into iron matrix more easily. So, they can be more coherent to the iron matrix with BCC crystal structure. This property can help copper particles infiltrate into iron matrix more efficiently to improve self-healing effects, even lower the sintering temperature. As a result, the shape and size of the additives such as copper affect the self-healing efficiency.

1.2.4 Materials preparation

Copper has the atomic number of 29, the density of 8.96 g/cm³, the atomic weight of 63.54, the melting point of 1083° C and the boiling point of 2570°C. According to the phase diagram of Fe-Cu shown in Figure 4, a solid solution of iron exists below 910°C with the ferrite (□) phase in the body-centered cubic (BCC) crystal structure, which is higher strength than the austenite (□) phase. Ferrite phase transforms to austenite phase at the temperature range between 910°C and 1394°C. Although copper and iron are not mutually soluble in both liquid and solid states, over 0.75% of copper can be introduced into the steel and increase the strength of SS samples.

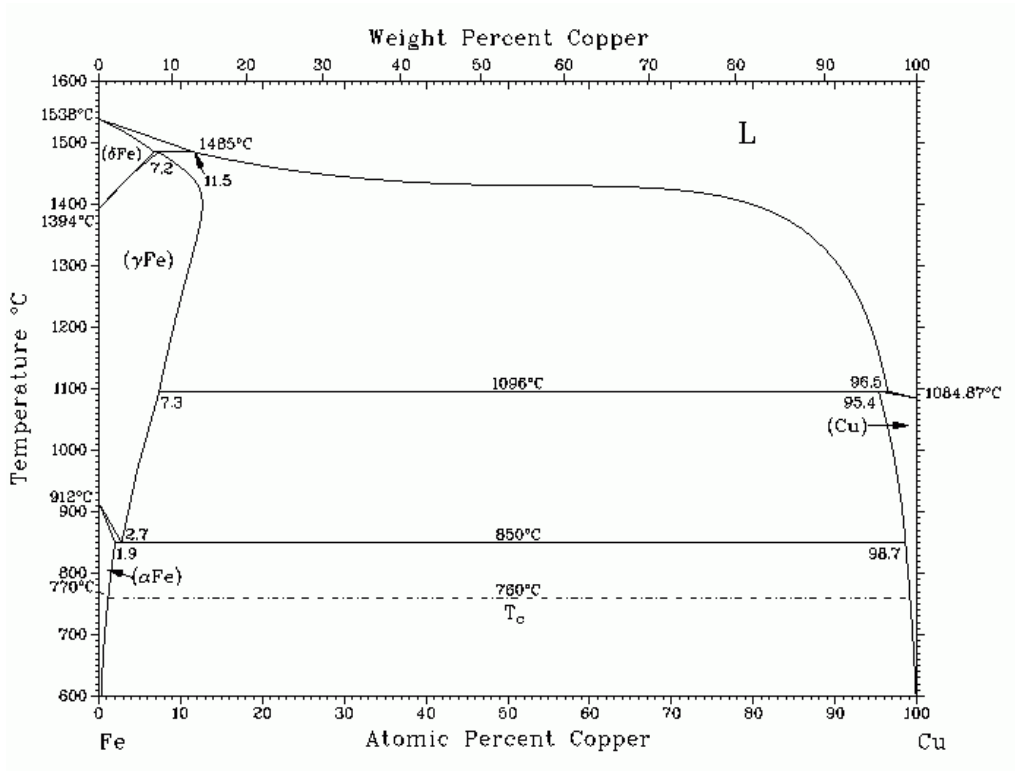


Figure 4. the relationship between Atomic percent and weight percent of copper in iron-copper alloy and temperature

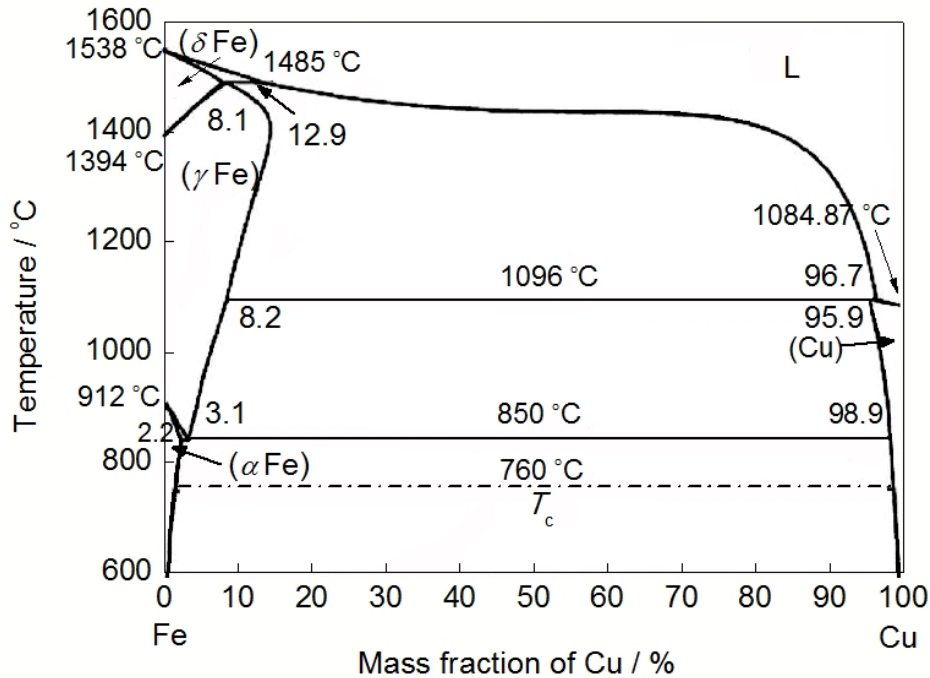


Figure 5. the relationship between mass fraction of copper in iron-copper alloy and temperature

Each phase of iron has distinct physical properties. In this research, we focus on the ferrite iron to study how copper can improve its strength. Figures 4 and 5 are the Cu-Fe phase diagrams which show the relationship between atomic percent, weight percent and mass fraction of copper in the iron-copper alloy as a function of temperature. From the Cu-Fe phase diagram, the maximum solubility of copper in the ferrite phase is 3.1% in mass fraction around 850°C. Thus, this amount of copper powder is mixed with SS powder in addition the boron powder which enhances sintering to achieve high dense specimens in this research. They are eventually heated to dissolve copper into the iron matrix to achieve “healing” effects, which will be demonstrated by the improved fatigue life in the fatigue testing. Moreover, the high-dense specimens as closed to the theoretical density of the steel parts fabricated by other traditional means are necessary in our fatigue test. The

0.5 w% of boron was found to be an ideal sintering additive to reach almost a full density of a SS part after 3D printing. The additional boron has no effect on the mechanical properties of specimens, which is also proved by experiments. All the experimental procedures will be described specifically later in this research. Since the copper should not be added over 3.1% (based on the phase diagram on Fig. 5), 3.08% of Cu was added into the SS powder in this study. The starting powder contains 3.08% of Cu, 0.5% of boron and 96.42% of SS powders, which has been premixed for 3D printing samples. The SS powder is however consisting of 60% a large powder and 40% of a smaller size to achieve a higher packing during the printing process [Do et al. 2017].

1.2.5 Properties of copper-iron alloy

This research is inspired because copper additives have already had lots of applications. Others added different amounts of copper to SS powder in order to modify the physical and chemical properties. Steel with 0.15-0.25% copper has two to four times atmosphere corrosion resistance than carbon steels [51]. The effects produced by copper are better than any other traditional elements, like Mn, P, Si, Ni and Cr. Moreover, the steel containing 1-2% copper has good resistance to sulfuric acid and nitro sulfuric acid, which is used in explosives manufacturing and paper industries [51]. The addition of 0.15-1.5% copper slightly increases the hardenability of steels while heat treatable cast steels rely on copper to improve fluidity. The addition of 2% copper raises the yielding strength by 130MPa and tensile strength by 90MPa while keeping the ductility unchanged [51]. Specifically, there are plenty of applications in powder metallurgy (P/M), where copper is added into iron [52]. The clutch hub for automatic transmission made with a copper-

infiltrated iron P/M part saves 25% cost compared with traditional forging method [52]. An automatic transmission part consisting of an SAE 1112 steel pin and a body of P/M iron infiltrated with copper had to meet medium shock, medium torque, load-bearing wear and high-strength requirements [52]. The pin was bonded to the body during sintering. The assembly was carbonitrided and hardened. After this treatment, the body had a tensile strength of 120 ksi (827 MPa) [52]. Furthermore, adding the copper powder into different types of iron powder can yield various changes in mechanical properties and the resulting dimension changes in P/M parts. For example, a low-carbon copper P/M steel is used for a projector sprocket. A similar steel is used for an automatic dryer belt adjustment. For the application, requiring high strength and impact resistance together with sufficient porosity for oil impregnation, a 2% copper-0.6% carbon steel was produced. [52]

Prealloyed powder obtained by atomizing a suitable iron or steel composition can also be used to produce P/M parts, to which metallic copper can be added by mixing them before compaction. Premixes of iron and copper, with or without graphite, are made by simple blending. These premixes can be fabricated to produce a wide variety of density and strength levels by conventional pressing and sintering. In this research, we focus on the effects of enhancement on the fatigue strength of 3D printing SS samples by mixing a small amount of copper.

1.2.6 Boron-additives effects on 420 stainless steel

A small amount of additives mixed into metal powder can improve the densification and structure integrity, lowering sintering temperature through the study of powder metallurgy (P/M) [35]. A series of experiments is carried out to determine the type of ingredient and the amount to be added in order to obtain the highest densification with the minimum sintering temperature for 420 SS powders. In our previous research [35], 0.5%, 1% and 1.5% percent powder of boron, boron nitride or boron carbide were mixed into the SS420 powder. Cubic samples are 3-D printed and sintered for the density test and compare the final density with samples without additives. The sintering temperature are set up as 1150°C, 1200°C and 1250°C and each sample sinter under these three temperatures. The relative densities of the samples sintered at 1150°C and 1200°C are around 50% to 80% respectively, which is disqualified for fatigue test. Also, the addition of 1.5% these additives generates the liquid phase extensively to distort the shape of samples which are not acceptable for 3D printing applications. At 1250°C, the relative density of samples with 1% of three additives is higher than 90%. The best one reaches 96% with the addition of 1% boron sintered at 1250°C. Based on this research results, we conclude that boron and boron nitride should be the two best additives for our SS420 powder at 1250°C. However, the required amount of boron additives and the sintering temperature must be adjusted to fabricate our self-healing samples as the copper powder must be added and mixed with SS420 powder.

Chapter 2 RESEARCH OBJECTIVES

There are several objectives in different stages of the experiments.

1. Determine the amount of copper powder mixed into SS420 powder based on copper-iron phase diagram in order to achieve the best mechanical properties and the subsequent fatigue test.
2. Investigate the best sintering additives, the mass fraction of additives and the sintering temperature for copper-iron mixtures to achieve at least over 95% relative density. A cube of $1\text{ cm} \times 1\text{ cm} \times 1\text{ cm}$ is modeled and fabricated by 3D printing for density measurement in this step.
3. The samples of $4.5\text{ cm} \times 0.69\text{ cm} \times 0.16\text{ cm}$ are printed for fatigue test. Each sample should have the identical dimension, density and surface finish. They will be cut into a dog-bone shape subsequently by Wire-Electro discharged machine (w-EDM). The S-N diagram will be constructed based on the fatigue test results.
4. The ultimate purpose is to investigate whether or not the addition of copper provides the self-healing of SS420 parts produced by 3D printing in our fatigue testing. As a reference, the samples without copper powder are also fabricated for the fatigue test.

5. The planned fatigue tests consisted of two distinct tests, the one to induce fatigue damage without failure and the other to fracture the sample. To induce the fatigue damage, the fatigue cycle is run for a certain number of cycles definitely below the fatigue life on at least two samples and after the initial fatigue cycle, these samples are heat-treated to heal the microscopic damages. The optimal heat treatment temperature should be determined. The second test is the fatigue test under the same stress till samples fails. The experimental data will prove that the fatigue life of samples with copper is improved much more than those without copper.

6. The fatigue results must be compared before and after the heat treatment and calculate the improvement in the life cycles on both types of samples.

Chapter 3 EXPERIMENT PROCESSES

3.1 Samples preparation

3.1.1 Powder additive amount

The spherical 420 SS powder (Ex-one, USA), copper powder and boron powder were used for this research. The 420 SS powder is the main powder whose size is between 20 μ m and 50 μ m with the average size of 30 μ m. The copper powder with the average size of 10 μ m is used to provide the healing of the consolidated stainless steel. The boron powder with the average size of 1 μ m is used as a sintering additive to consolidate the powder mixture to a near full density.

Six tests were performed to reach the maximum density in our samples with different amounts of additives and sintering temperature.

Experiment number	Additives	Sintering temperature/ $^{\circ}$ C	Sintering time/hours
1	96.92% large SS 420, 3.08% Cu	1250	6
2	96.92% large SS 420, 3.08% Cu	1300	6

Table 1: six experiments with different additives in different sintering temperature to obtain full dense samples

Table 1 (cont'd)

3	99% large SS 420, 1% Cu	1350	6
	96.92% large SS 420, 3.08% Cu	1350	6
4	95.92% large SS 420, 3.08% Cu, 1% BN	1300	6
5	powder 57.852% large SS 420, 38.568% small SS 420, 3.08% Cu, 0.5% boron	1250	6
6	57.852% large SS 420, 38.568% small SS 420, 3.08% Cu, 0.5% boron	1150	6

For each test, the powders are mixed uniformly by the high-speed mixer (DAC 150.1 FVZ, FlackTek inc., Landrum, SC, USA) which is capable to vary the speed between 300 and 3500 rpm. Only two minutes are usually enough for mixing them uniformly. The MRF (Materials Research Furnaces) environment-controlled furnace is applied to sinter the samples. The vacuum or argon gas environment can be provided to prevent the oxidation of samples. Vacuum environment is found to be better to improve the final density. Different sintering temperature and additives are chosen in this experiment to compare the final densities in order to optimize the sintering condition. Before the sintering process, the samples are heated to 240°C at a rate of 10°C/min and kept for two hours in air furnace to burn out the binder phase which consists of Ethylene Glycol Monobutyl Ether, Ethylene Glycol and Isopropanol. Each of these binder constituents is burn out the temperatures of 170°C, 197.3°C or 82.6°C, respectively. In the subsequent sintering process, the samples will be heated from 240°C at a rate of 5°C/min to a preset sintering temperature. Once the preset sintering temperature is reached, the furnace was kept at this temperature for six hours to complete the sintering process. The final step is to cool down samples to room temperature at a rate of 10°C/min. Table 1 shows that the samples with different combinations of additives, including without any sintering additive, are sintered between 1150°C and 1350°C. The relative density measurements will be measured using Archimedes method to determine optimal processing conditions.

3.1.2 Printing

The X1-Lab 3D printer is used in all of our 3D printing process. Basically, two printing beds, a supply bed and a printing bed, exist in the X1-Lab. The supply bed has the movable base which pushes a right amount of powder to fill a layer of powder into the printing bed. The powder from the supply bed is pushed to the printing bed by the roller which maintains the smooth layer of the powder on the printing bed. When the printing process begins, the roller moves a layer of powder which is set at 0.1 mm from the supply bed to the printing bed. Then, the binder phase is applied selectively on this layer before preparing for next layer. During this process, obviously the supply bed is raised up and printing bed is lowered when printing in a layer by layer fashion. Binder phase must keep every layered section to stick together. The printed samples are very fragile, which must be cured to stabilize the shapes. This process maintains the shape of samples before burning out the binder phase.

3.1.3 Curing

The curing process cures the binder phased on the printed samples in a curing furnace at 195°C for 2 hours to stabilize the shapes. Otherwise, the samples will be too fragile to handle other subsequent processes.

3.1.4 Sintering

The environment-controlled furnace is applied to sinter the samples after printing subsequent to the binder burnout. The argon gas or vacuum environment prevents the oxidization of samples.

For our experiment, vacuum environment is chosen to improve the final density. In sintering process, the samples are heated to preset temperature, for example, 1150°C. Once the preset temperature is reached, the furnace maintains this temperature for 6 hours. The final step is to cool down to room temperature again. In this research, 1150°C is the lowest sintering temperature used. It is better to achieve a higher density at a lower sintering temperature to minimize the any shape distortion.

3.1.5 Shapes and density test

Because the dimension of samples is hard to be measured accurately, Archimedes' principle is applied to calculate the density of samples, which indicates that upward buoyant force is equal to the weight of the fluid that the body displaces. The formula is following:

$$F_b = \rho_w g V_w$$

In our case, we measure the mass m_1 in air and the mass m_2 of samples which are fully submerged into water.

ρ_w =the density of water

V_w =the volume of water displaced by the sample

Based on Archimedes' principle, we can deduct the relationship of between m_1 and m_2

$$F_b = \rho_w g V_w$$

$$m_b \rho_w = \rho_w g V_w$$

$$m_b = g V_w$$

$$m_1 - m_2 = g V_w$$

The volume of water displaced by sample:

$$V_w = \frac{m_1 - m_2}{g}$$

Since the volume of water displaced by sample is the same with the volume of the sample, so

$$V_w = V_1$$

The density of the sample is

$$\rho_1 = \frac{m_1}{V_1}$$

For the powders used in the experiments, the density of the material for each powder is shown below:

Additives	Density (g/cm ³)	Particle size (μm)	Provider
Large 420 SS powder	7.740	30	EX-one
Small 420 SS powder	7.740	6	Atmix
Copper powder	8.900	10	Alfa Aesa
Water	0.998	N/A	N/A
Boron Nitrite powder	2.290	1	Sigma Aldrich
Boron powder	2.370	1	Sigma Aldrich

Table 2: density of additives used in this research

The calculated densities of all samples in six experiments are shown in table:

Experiments run number	Samples number	Mass (g)	Volume (cm ³)	Density(g/cm ³)	Relative density (%)
1	1	2.591	0.453	5.710	73.48
	2	2.576	0.385	6.695	86.15

Table 3: the density and relative density of six experiments which are to obtain full dense sample

Table 3 (cont'd)

2	1	2.670	0.366	7.305	94.00
	2	2.604	0.354	7.331	94.33
3	1	2.306	0.341	6.766	87.30
	2	2.258	0.336	6.723	86.75
	3	2.394	0.355	6.707	86.30
	4	2.415	0.349	6.884	88.58
4	1	3.929	0.538	7.299	96.17
	2	3.809	0.532	7.154	94.27
	3	3.874	0.525	7.379	97.22
	4	3.881	0.538	7.206	94.94
5	1	4.742	0.621	7.636	99.37
	2	4.741	0.622	7.628	99.28
6	1	4.610	0.603	7.645	99.49
	2	4.715	0.616	7.653	99.59

The samples were produced to reach the consistent high density before printing the specimens for fatigue test. Samples are all small cubes to minimize the powder usage and to measure their dimensions easily. Table 3 shows the results of the experiments described in Table 1. On the experiment number between 1 and 3, the powder mixtures of SS and copper without any sintering

additive were used. Despite of the increase in the sintering temperature from 1250°C to 1350°C, the relative density did not improve. With the additional copper, the final density did not improve even with the increase in the sintering temperature. The results from the first three experiments show that the sintering temperature of 1300°C is adequate to sinter our samples. Based on our previous work [35], 1% of boron nitride is added in the experiment run #4 at 1300°C, which substantially improve the relative density. However, the 3% variation in density from 94% to 97% among the experiment number 4 is still too much. Even though the density is high enough, a full-density 3D printed material is not necessary to prove the self-healing of copper. In the experiment number 5, two different sizes of 420 SS and 0.5% boron are utilized to achieve the particles in printing. The large stainless-steel powder from Ex-one, USA has the average particle size of 30µm and the smaller one from Atmix has the average particle size of 6µm. The mixture of the large and small powders leads to the final parts with almost full density consistently. Considering the energy consumption, sintering temperature must be reduced to 1150°C in the experiment number 6 with the same constituents as the experiment number 5 achieving the equivalent final density. As a result, the ideal powder mixture is determined to be 57.852% of large SS 420, 38.568% of small SS 420, 3.08% of Cu and 0.5% of boron powders, which is sintered at 1150°C for 6 hours. The resulting cubic samples are shown in Figure 6.

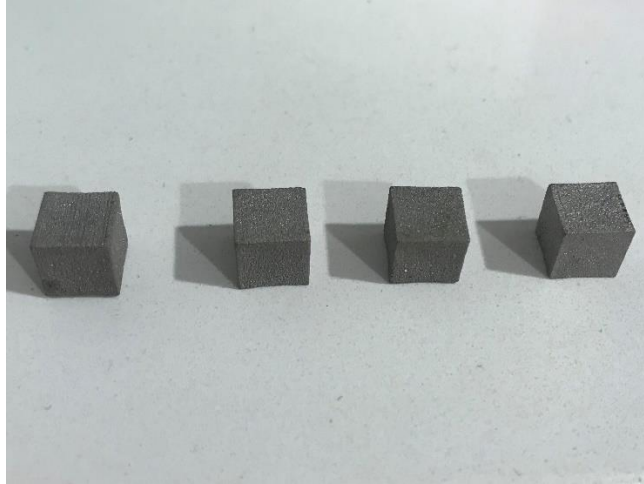


Figure 6. cubic samples after sintering under 1150°C for 6 hours

3.2 Specimens preparation and processes of fatigue test

3.2.1 Specimens printing

Cubic samples are printed and sintered to find out the best powder combination, which resulted in high-density samples consistently. With this information, total twenty plates with the dimension of 4.5cm x 0.69 cm x 0.16 cm are printed for the fatigue testing. In addition, one set of reference blocks without copper powder are fabricated for comparison. After sintering under the same condition, these plates require additional processes such as grinding, wire EDM and polishing to yield the dog-bone samples for fatigue test.

3.2.2 Grinding

Grinding is required to reduce the effort in polishing. Basically, the surface grinding uses a rotating abrasive wheel to remove material to create a flat surface. The surface quality of the sintering samples cannot meet the requirements for fatigue test. Grinding machine has an abrasive wheel, where a work piece is held on a reciprocating table electromagnetically. All the samples were ground in the same condition to obtain the consistent surface finish. However, the surface finish after grinding is still not qualified for fatigue test. Better surface finish has to be obtained by additional polishing.

3.2.3 Surface finish processing

After sintering, the specimens consistently have the density of at least 99.2%. However, the surface quality is too rough to conduct the fatigue test. First, both upper and lower surfaces are ground to attain the surface roughness between 0.3 and 0.6 μm , which is too rough for the fatigue testing. When the fatigue cycle is extended to very high cycles, the fatigue testing results are more sensitive to many factors such as specimen size and surface roughness. The surface finish of the higher strength materials such as SS will affect the fatigue behavior. The research data indicated that the fatigue life of the specimens with the surface finish of 0.74 μm surface is reduced compared to the specimens with the surface finish of 0.3 μm at the same stress amplitude condition [53]. Thus, the surface roughness affects the fatigue behavior of the specimens [53]. As the purpose of this research is not attaining the perfect surface finish, the 320-grit sandpaper is chosen to keep the surface finish consistent for all samples. The polishing procedure requires to keep the surface flat

and horizontal. After completing the polishing, the surface roughness of our samples was consistently between 30 and 40 nm.

3.2.4 WEDM

The samples must be cut into dog-bone shape samples for fatigue test. WEDM is used in this case. This method is usually for machining hard metals, as thick as 300 mm plate and typically used in industry to make punches, tools, dies and so on. A thin single-strand metal wire, usually brass, is fed through the workpiece, submerged in a tank of dielectric fluid. It is held between upper and lower diamond guides, which are CNC-controlled to cut the samples very precisely with the error less than 0.004mm and the kerf as small as 0.021mm. The dimension of our samples is showing below in Figure 7.

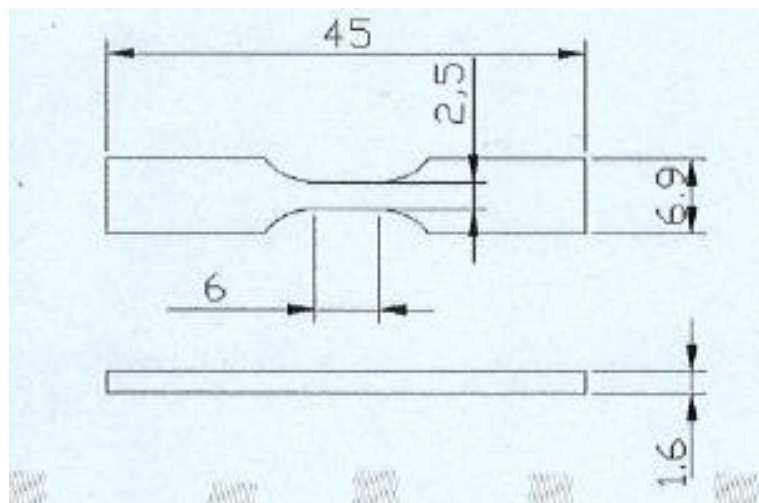


Figure 7. the dimension of samples with dog-bond shape for fatigue test

3.2.5 Fatigue test

Sample without copper are needed for comparisons. After preparing the samples for the fatigue test, four samples will be used for ultimate tensile strength (UTS) test and eight samples are used to construct the S-N diagram. The determination of UTS enable us to limit the highest stress applicable for the fatigue test. To construct the S-N diagram, multiple stress levels below UTS must be applied to our samples. The fatigue life cycles are recorded until the failure occurs on the samples loaded at different stress levels. The endurance limit is reached if no failure occurs no matter how many numbers of cycles applied below a certain stress threshold. S-N diagrams are plotted against two variables, magnitude of alternating stress and the number of cycles to failure. The results are usually displayed on logarithmic scales. The S-N diagrams should be built for the healable samples as well as the reference samples. Based on the S-N diagram, two stress levels in the middle range of the fatigue test undergoes about 70% percent of the allowable stress cycle. As a result, the samples attain some microscopic damages such as cracks and voids without failure. Then, these samples after heat-treating for self-healing are put to the fatigue test again until they fail under the cyclic load. The life cycles are recorded until it breaks, which are compared with the life cycle without the heat treatment under the same stress. By comparing the results, we can determine if the immigration of copper atoms can 'heal' those cracks and voids. Also, the same heat treatment process and fatigue tests are applied to the reference samples without copper to determine the effect of copper. The broken sample after the fatigue test is shown in Figure 8.

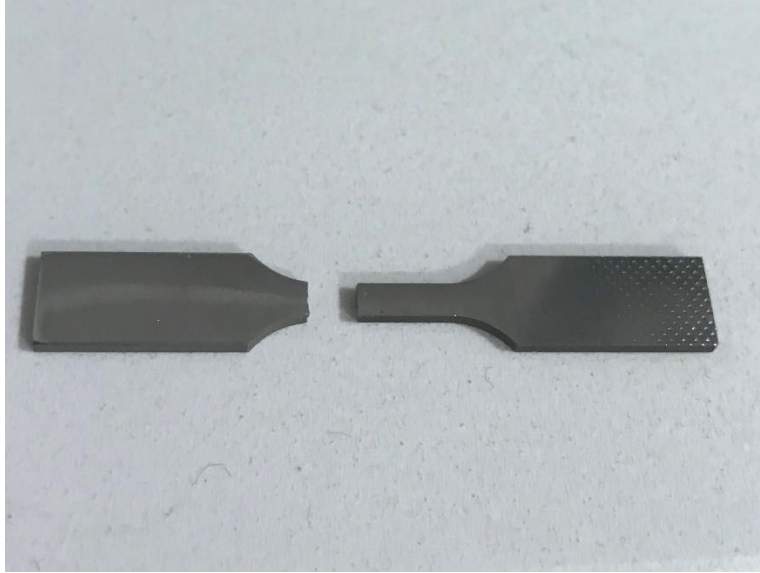


Figure 8. A broken sample after fatigue test

3.2.6 Heat treatment

Based on the Fe-Cu phase diagram, the heat treatment cycle is determined to be 950°C , where the phase transformation of iron allows the copper atoms to diffuse into the iron matrix and heal the microscopic damages. This is the annealing process used in industries. Annealing alters the physical and sometimes chemical properties of a material to increase its ductility and reduce its hardness for subsequent deformation processing. In our case, the temperature of 950°C is needed to transform the iron phase from ferrite to austenite. During the annealing, iron atoms migrate in the crystal lattice and the number of dislocations decreases, leading to the change in ductility and hardness, which means that the samples will heal itself even without the presence of copper. That makes the reference samples necessary in our study. Theoretically, the fatigue life of the samples without copper should be increased after annealing. The extend of the improvements

in the fatigue life for both samples should be compared after heating at 950°C to prove the healing effects by the presence of copper.

Chapter 4 RESULT DISSCUSION AND ANALYSIS

4.1 S-N diagram

4.1.1 UTS testing

After the fatigue test, the results on UTS test and stress versus fatigue life cycles (S-N diagram) are recorded and compared for both materials. Multiple stresses levels below UTS is selected to create S-N diagram. The endurance limit, typically taken as 0.5 of UTS were different on our samples. Because the endurance limit means the stress below which the fatigue failure will not occur, the endurance limit can be determined experimentally.

Material	UTS (MPa)	Endurance limit (MPa)
Without copper	787	275
With copper	833	333

Table 4: UTS test result for sample with copper and without copper

Table 4 show that the UTS of the sample with copper is slightly higher than that without copper. Obviously, these two different materials have different S-N diagrams. The samples with copper are called healable materials and the samples without copper are standard materials.

4.1.2 Stress and life cycle for healable samples

stress (MPa)	number of cycles	number of cycles (in the logarithmic scale)
583	20980	4.32
540	19191	4.28
483	70520	4.84
458	66307	4.82
416	88090	4.94
390	83058	4.91
366	219469	5.34
333	1000000	6
333	280000	5.44
333	1300000	6.11
333	1500000	6.17
333	1800000	6.25
333	2000000	6.30
333	10000000	7

Table 5: stress and life cycle for samples with copper

Table 5 shows all the fatigue results. The stress for the healable samples of the fatigue test started with 585 MPa and obviously the stress of 333 MPa is equal or less than the endurance limit. When plotting the S-N diagram, stress and number of cycles are usually displayed on the logarithmic scale. In this case, the fatigue results from Table 5 are plotted in Figure 9 where the experimental data points are the result of the fatigue tests. Figure 9 also has the red linear trend line through all the data points as S-N curve of healable materials and the blue point indicates the endurance limit.

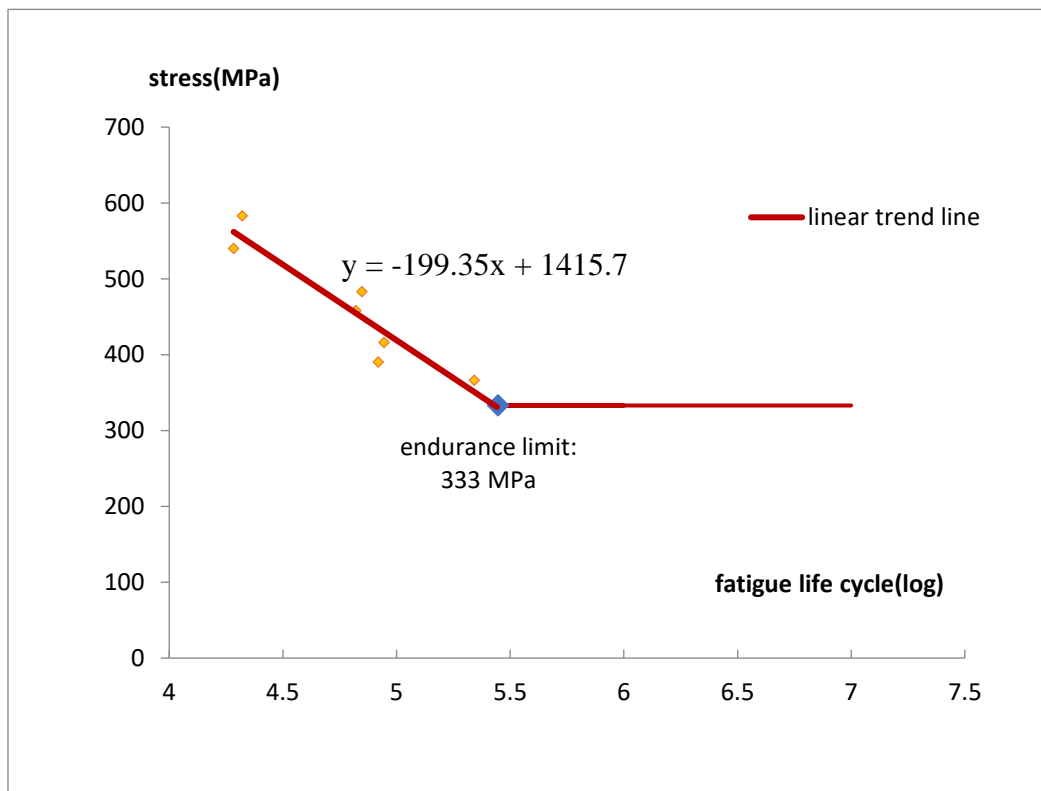


Figure 9. S-N diagram for samples with copper (healable sample)

With the red trend line in Figure 9, we were able to select the life cycles with the stresses at 450 and 380 MPa, which are in the middle range of stress in S-N diagram. So, we also calculate the 70%, 80% and 85% life cycles under these two stresses. At the beginning, tensile test is carried

out on our samples below 70% life cycles under these two stresses, which should create the microscopic damages in the samples. The heat treatment should heal the damages in the samples. From the S-N diagram in Figure 9, the data points are actually slightly scattered. 80% and 85% life cycles are considered too high and probably result in failure of samples. Unfortunately, the samples are broken after 50% and 60% of the life cycles under these two stresses respectively. Thus, the initial fatigue cycle was run up to 90000 cycles which is 40% of the fatigue life.

stress (MPa)	life cycle(log)	life cycle
450	4.84	69862.44
380	5.19	156814.06

Table 6: life cycle of samples with copper at 450 and 380 MPa

Table 6 shows the fatigue life cycles of the healable material under the stress level of 450 and 380 MPa. In Figure 9, the fatigue data points are scattered and some samples are broken even at 50% and 60% percent before heat treatment. Therefore, it was chosen to run the 40% of the fatigue life cycle under 450 and 380 MPa for the additional fatigue test.

stress (MPa)	70% life cycle (log)	80% life cycle (log)	85% life cycle (log)	70% life cycle	80% life cycle	85% life cycle
450	3.39	3.87	4.11	48903.71	55889.95	59383.07
380	3.63	4.15	4.41	109769.84	125451.24	133291.95

Table 7: life cycle of samples with copper at 450 and 380 MPa for red linear trend line

Table 7 contains the 70%, 80% and 85% of the fatigue life cycles under 450 and 380MPa. As mentioned before, with the failure of some samples before reaching 70% of fatigue life cycle, less than 70% of the fatigue life cycles have to be applied.

4.1.3 Stress and life cycle for standard samples

stress (MPa)	life cycle	life cycle(log)
550.9	36056	4.55
472.2	78511	4.89
407	142105	5.15
354.15	250000	5.39
354.15	1000000	6
354.15	2000000	6.30
354.15	2500000	6.39
354.15	3000000	6.47
354.15	3500000	6.54

Table 8: stress and life cycle for samples without copper

Table 8 demonstrates the fatigue test results for the standard samples to plot a S-N diagram. The test is started from 550 MPa. With the endurance limit of 354 MPa, the standard sample cannot undergo fatigue failure at the stress below this limit.

stress (MPa)	linear life cycle(log)	line life cycle
450	4.97	95292.49
380	5.26	185923.56

Table 9: life cycle of samples without copper at 450 and 380 MPa

Stress (MPa)	70% life cycle (log)	80% life cycle (log)	85% life cycle (log)	70% life cycle	80% life cycle	85% life cycle
450	3.48	3.98	4.23	66704.74	76233.99	80998.61
380	3.68	4.21	4.47	130146.49	148738.85	158035.03

Table 10: life cycle of samples without copper at 450 and 380 MPa for linear line

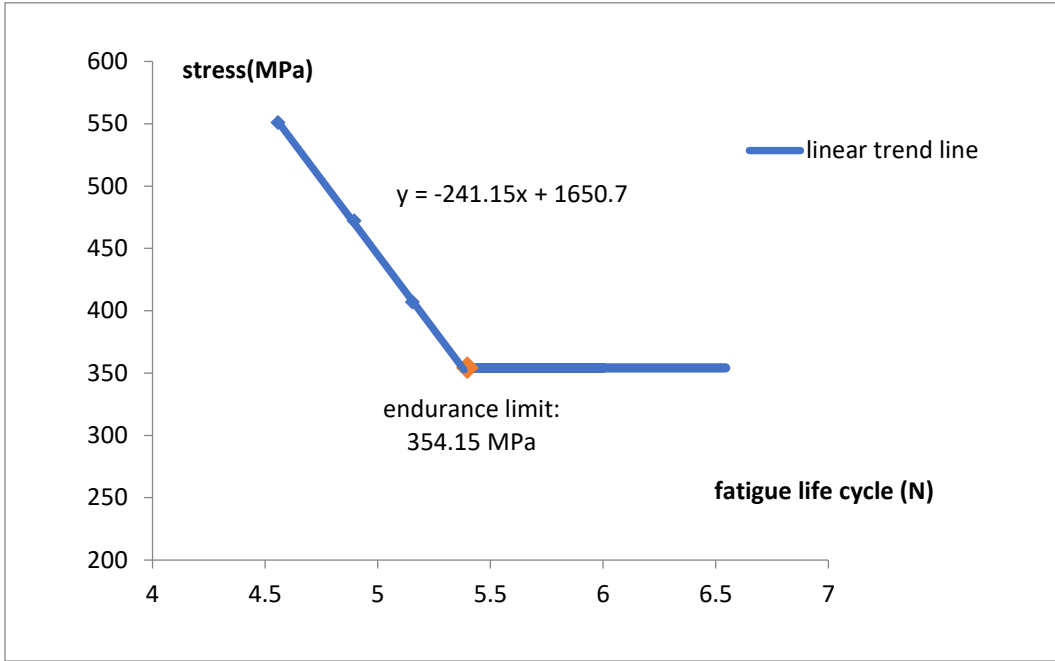


Figure 10. S-N diagram for samples without copper (standard sample)

Tables 8-10 and Figure 10 are obtained for the standard samples without copper. Basically, the S-N curve is linear as shown in Figure 10. The 70%, 80% and 85% percent of the fatigue life cycles under the same stress are calculated as did for the healable samples shown on Table 9 and 10. For the standard samples, the variation is much smaller. To make sure the survival of the samples under the initial fatigue test, the 50% of the fatigue life cycles on the standard samples without copper will be chosen for fatigue test under 450 and 380 MPa for fatigue test.

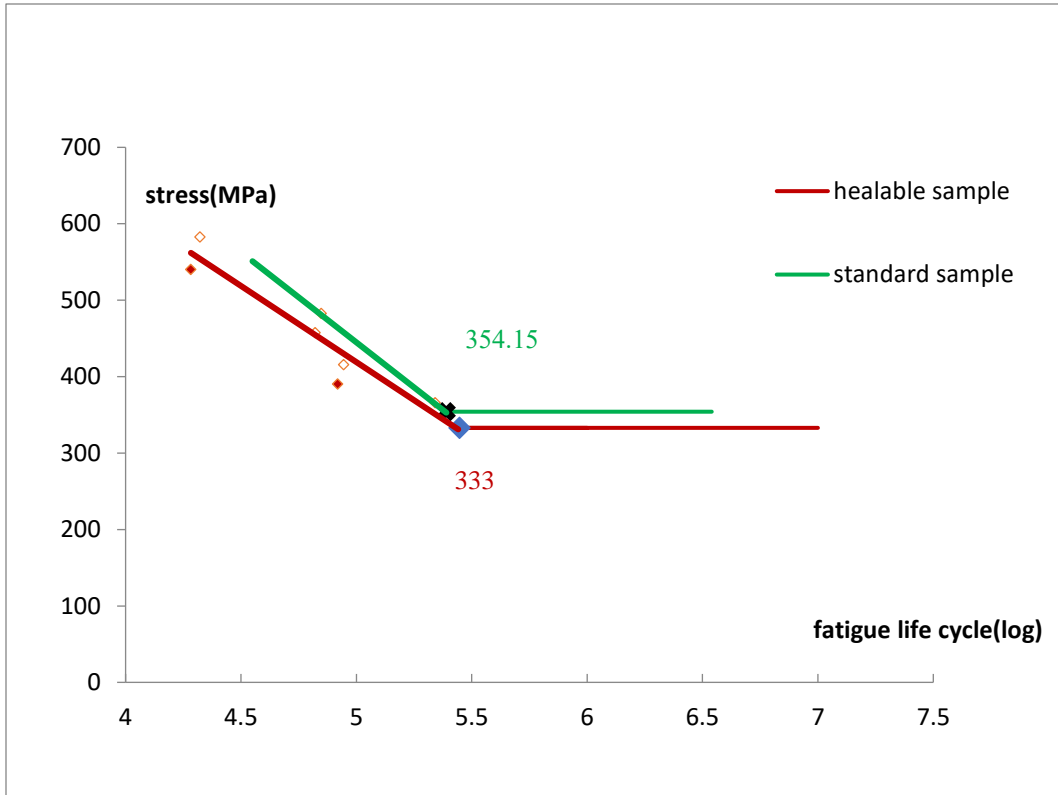


Figure 11. S-N diagram for healable sample and standard sample

Figure 11 was presented by superimposing Figures 9 and 10 to compare the S-N diagrams of the healable and standard samples. Two S-N curves are slightly different with the standard samples with a slightly higher endurance limit than the healable samples. Also, the level of stresses we select for the fatigue test before heat treatment, 450 MPa and 380 MPa, are in the middle range of stresses in both of S-N diagrams.

After the fatigue tests, heat treatment was carried out on all the samples at 950°C for 2 hours. During the heat treatment, the copper atoms are expected to diffuse into the iron matrix to heal the microscopic damages, which enable us to achieve “self-healing”.

4.2 Result of improvement of fatigue life after healing

Materials	Stress (MPa)	Life cycles before heat treatment	Life cycles after heat treatment	Increasing rate
Reference samples (without copper)	551	10915	10915+530	4.86%
	472	44435	44435+44190	99.45%
	407	79019	79019+76274	96.53%
Healable samples	419	86893	86893+118147	135.97%
	366	94518	1000000	Increase endurance limit

Table 11: life cycles of both types of samples before and after heat treatment to reflect the improvement on fatigue behavior

The fatigue life cycles of the standard samples without copper are increased by almost 100% because of the annealing effect while the fatigue life cycle is enhanced by 136% for the healable samples. The difference of 36% improvement in fatigue life is equivalent to 31281 cycles between two samples. It can even reach up to the endurance limit and increase the endurance limit from 333 MPa to 366 MPa. Therefore, the copper definitely improves the fatigue life of SS-420 fabricated through the 3D printing technology.

4.3 SEM images

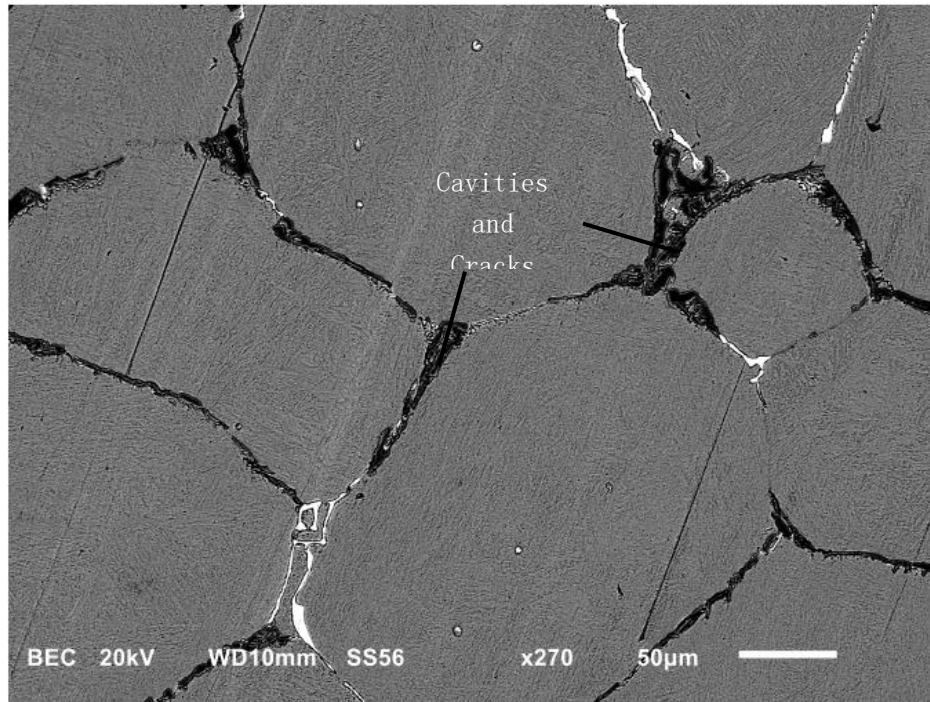


Figure 12. image of grain boundaries of samples without copper

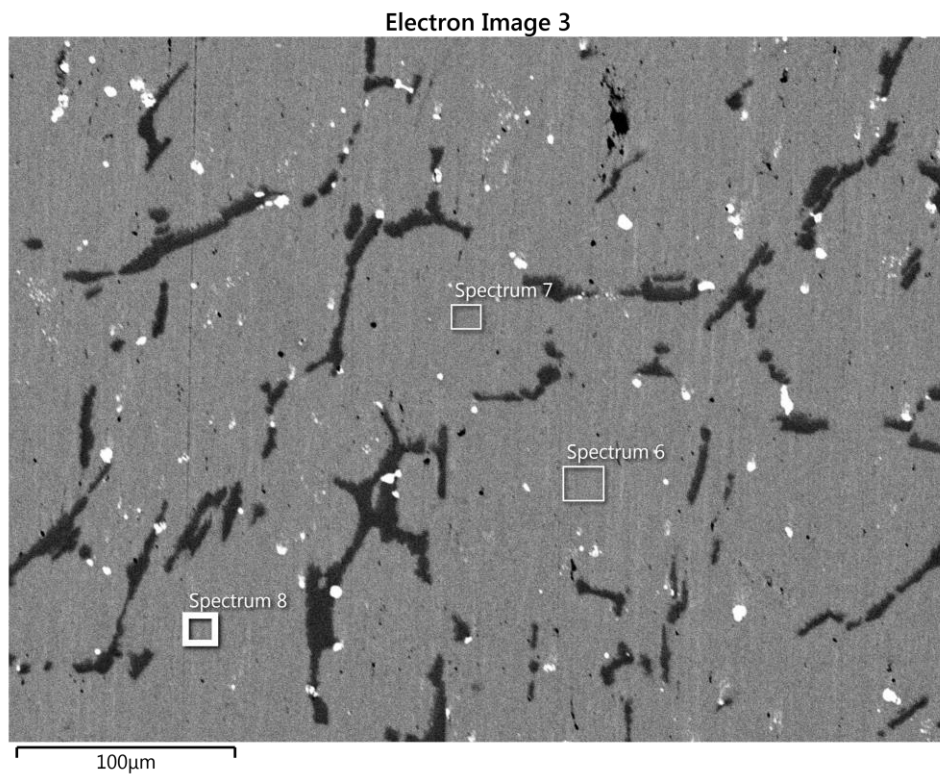


Figure 13. image of grain boundaries of samples with copper

We can see the grain boundaries of our standard and healable samples in Figures 12 and 13, respectively. As can be seen in Figure 12, the sample without copper has wider grain boundaries between grains which are shown as black areas. The SEM images show the defects of grain boundaries are reduced in the healable samples with copper. As a result, copper can achieve healing effect for SS420 from structure analysis.

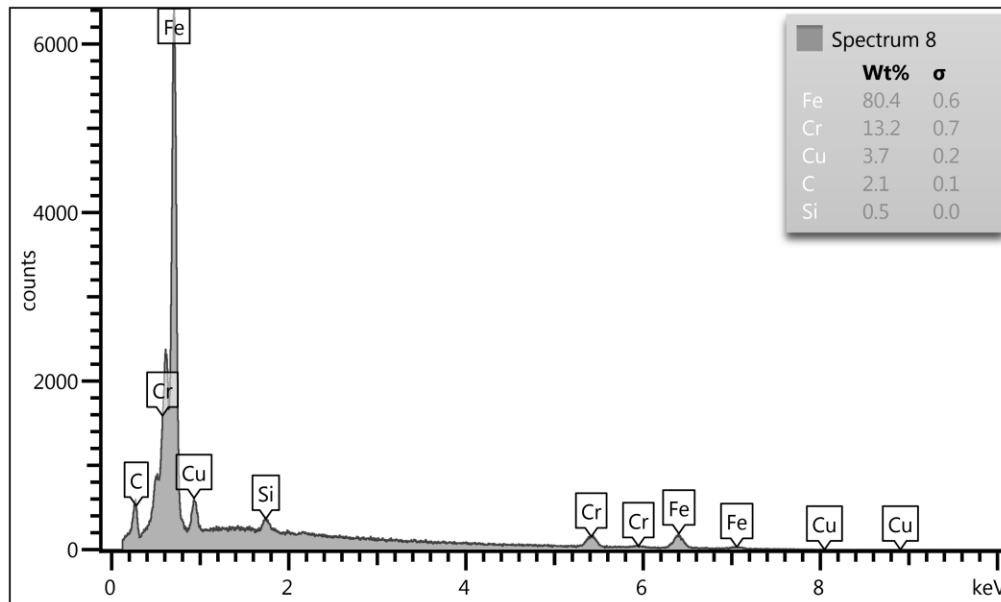


Figure 14. percentage of all elements in random spot picked in SEM image

A small area on the SEM image is observed to detect the elements on our samples. We can see most of them are iron (80.4%) with 3.7% copper and some other elements as shown in Figure 14. To analysis the spatial distribution of each element, we put colors on different elements to show the elemental distributions on Figure 15. The first image of Figure 15 shows small amounts of carbon atoms in SS420 samples. The fourth image indicate that iron atoms are the major element in the samples. The fifth image tells that the copper atoms are diffused into everywhere with some

other elements like niobium mixed into the samples during the polishing process from sandpapers and grinding which have no effects to the results.

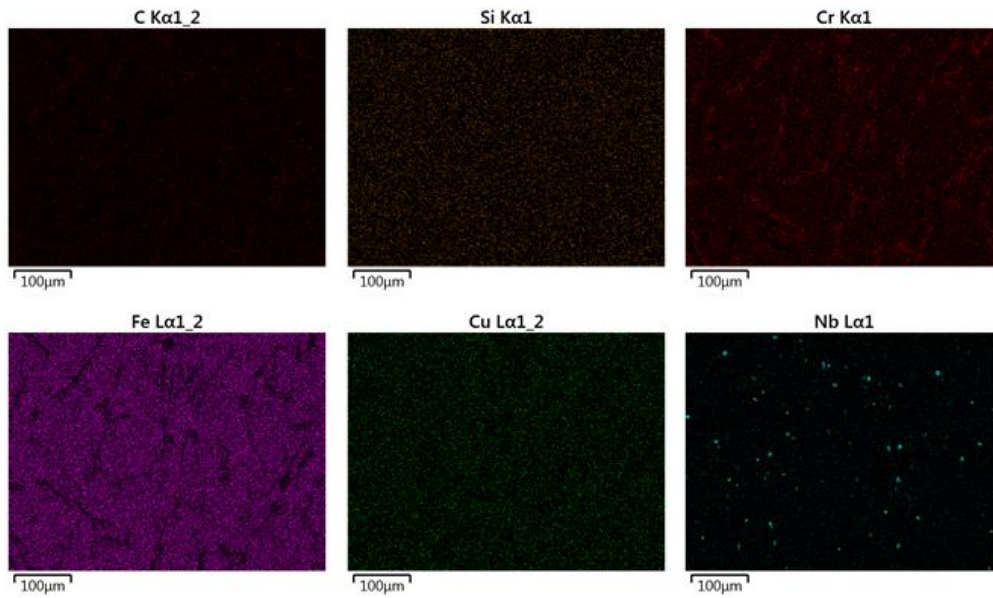


Figure 15. the distribution of all elements in the spot picked

Chapter 5 CONCLUSIONS

5.1 Difficulties and problems

The ideal powder combination and sintering temperature were hard to obtain to reach the high density in our 3D printed samples. The production of specimens for our mechanical testing was a time-consuming process as many samples were damaged and consumed during sintering, WEDM process and fatigue test. Many of the healable specimens were broken after only 60% or 70% of the fatigue life cycles under 450 and 380 MPa. It is recommended that fewer life cycles should be run for fatigue test before heat treatment.

5.2 Data analysis and conclusions

The desired microstructure consisting of mainly iron phases with a small amount of copper (3% copper and 96.5% SS powder) are attained by using 3D printing. The 0.5% boron was added to enhance sintering the SS powder. Twenty rectangle blocks with 4.5cmx0.69cmx0.16cm are printed as fatigue samples. After curing and sintering, the final samples have the final density of at least 99.2%. After the samples are printed, the surfaces were polished to attain the consistent surfaces for the fatigue tests. Surfaces roughness of the all samples falls between 0.3 to 0.5 micrometers after grinding, however, it can reach to 0.03 micrometers after polishing by using 320 grits sandpaper. Afterwards, the samples are cut with w-EDM to fabricate the dog-bone shaped samples for fatigue test to construct S-N diagram. The specimens are cyclically loaded below the number of cycles to failure under certain stresses. Based on the Fe-Cu phase diagram, the specimens is

heated up to 950°C for two hours for the healing treatment, and then the fatigue test conducted again under the same stress to prove the increase in the number of cycles by healing. As a result, the addition of a small amount of copper contributes to heal the SS sample fabricated by 3D printing.

The detailed conclusions attained during this research are listed as follows:

1. The use of boron additive can enhance the sintering density and reduce the sintering temperature. With the SS powers used in this study, the addition of 0.5% boron enhances the density to 99.2% relative density and reduces the sintering temperature to 1150 °C.
2. The samples without Cu and B can only achieve the densities between 73% to 86% under the sintering temperature of 1250°C. The powder mixture of 57.852% of larger SS 420 (the particle mean size of 30µm), 38.568% of smaller SS 420 (the particle mean size of 6µm), 3.08% Cu and 0.5% boron is printed and reached the maximum density of 99.2% after subsequent sintering at 1150 °C for 6 hours. The packing after printing is improved with the addition of a smaller size particles among larger size particles.
3. The number of fatigue life cycles under specified stress levels is increased for the samples with copper after heat treatment much more than the samples without copper. For the specimens without copper, the fatigue life cycles are increased after heat treatment from 44435 to 88625 cycles under 472 MPa by 99.45% and from 79019 to 155293 cycles under

407 MPa by 96.53% due to annealing effect. For the healable specimen with 3% Cu powder additives, the fatigue life cycles can be improved from 86893 to 205040 cycles under 419 MPa by 135.97%. In addition, the addition of copper also slightly increases the endurance limit from 333 MPa to 366 MPa. The healable specimens have 36% improvement in fatigue life equivalent to 31281 cycles by comparing the results of fatigue life cycles of standard specimens. Thus, copper definitely improves the fatigue life of SS-420 fabricated through the 3-D printing technology.

In conclusion, the addition of Cu (3.08%) makes the precipitates at the grain boundaries which repairs the crack during heat treatment, possessing the self-healing property for 3-D printed SS parts.

BIBLIOGRAPHY

BIBLIOGRAPHY

1. https://marketing.metatek.com/smartblog/sand_casting_process_advantages_and_limitations
2. <https://me-mechanicalengineering.com/casting-process-advantages-and-limitations/>
3. <http://www.monarchmetal.com/blog/3d-printing-metal-the-advantages-of-direct-metal-laser-sintering/>
4. ASTM, F2792-12a. (2012). Standard Terminology for Additive Manufacturing Technologies. ASTM International. West Conshohocken, Pennsylvania.
5. Huang, S.H., et al., (2013). Additive manufacturing and its societal impact: A literature review. International Journal of Advanced Manufacturing Technology. 67(5-8): p. 1191-1203.
6. Peng T., (2016). Analysis of Energy Utilization in 3D Printing Processes. Procedia CIRP. 40, 62-67.
7. Lipson H., & Kurman M., Fabricated: The New World of 3D Printing. Indiana: John Wiley & Sons, Inc.; p. 11.
8. David Bak, (2013). Assembly Automation. Volume 23 Number 4. pp. 340–345
9. Martin J. H. et al, (2017). 3D printing of high-strength aluminum alloys. Nature. 549, 365.
10. <https://blog.dragoninnovation.com/2014/12/30/top-10-benefits-3d-printing-salient-technologies/>
11. Lewandowski, J. J. & Seifi, M. (2016). Metal additive manufacturing: a review of mechanical properties. Annu. Rev. Mater. Res. 46, 151–186.
12. Frazier, W. E. (2014). Metal additive manufacturing: a review. J. Mater. Eng. Perform. 23, 1917–1928
13. Gramsma M. E., Self-healing of deformation-induced defects in Fe-based alloys using positron annihilation techniques. Msc thesis. Delft university of technology.

14. Zhang S. S., Self-healing of damage in Fe-based alloys. Ph.D thesis. Technische Universiteit Delft.
15. Laha K, Kyono J, Kishimoto S, Shinya N., (2005). *Scr Mater.* 52:675.
16. Laha K, Kyono J, Shinya N., (2007). *Scr. Mater.* 56:915.
17. Laha K, Kyono J, Shinya N., (2007). *Philos. Mag.*, 87:2487.
18. Shinya N., In: van der Zwaag S, editor. (2007). Self-healing materials: an alternative approach to 20 centuries of materials science. Dordrecht: Springer,
19. Laha K, Kyono J, Shinya N., (2012). *Metall. Mater. Trans. A*, 43A:1187.
20. He S. M., van Dijk N. H., Schut H., Peekstok E. R., van der Zwang S., (2010). *Phys. Rev. B*, 81:094103.
21. He S. M., van Dijk N. H., Paladugu M., Schut H., Kohlbrecher J., Tichelaar F. D., van der Zwang S., (2010). *Phys. Rev. B*, 82:174111.
22. Marian J, Wirth B. D., Odette G. R., Perlado J. M., (2004). *Comp. Mater. Sci.*, 31:347.
23. Soisson F., Fu C. C., (2007). *Phys. Rev. B*, 76:214102.
24. Aissa B., Therriault D., Haddad E., and Jamroz W., (2012). *Adv. Mater. Sci. Engin.* 2012:854203.
25. Yuan Y. C., Rong M. Z., Zhang M. Q., Yang G. C. (2009). Polymer. 50:5771.
26. Grabowski B. Tasan C. C. Self-healing metals, in book: *Advances in polymer science*.
27. Shinya N, Kyono J, Laha K. (2006). Self-healing effect of boron nitride precipitation on creep cavitation in austenitic stainless steel. *J Intell Mater Syst Struct* 17:1127.
28. Wright MC, Manuel MV, Wallace T. (2013). Fatigue resistance of liquid-assisted self-repairing aluminum alloys reinforced with shape memory alloys. NASA/TM-2013-216629. National Aeronautics and Space Administration, Hampton.
29. Rohatgi PK. (2014). Al-shape memory alloy self-healing metal matrix composite. *Mat Sci Eng A Struct* 619:73.

30. Ferguson JB, Schultz BF, Rohatgi PK. (2015). Zinc alloy ZA-8/shape memory alloy self-healing metal matrix composite. *Mat Sci Eng A Struct* 620:85.
31. Lucci JM, Rohatgi PK, Schultz B (2008). Experiment and computational analysis of self-healing in an aluminum alloy. In: Proceedings of the ASME international mechanical engineering congress and exposition. Boston, USA.
32. He S. M., Brandhoff P. N., Schut H., van der Zwaag S., van Dijk N. H., *J. Mater. Sci.*, 2013, 48: 6150.
33. Copper Development Association Inc. (2013, August 12). Copper in Iron and Steel P/M Parts. UK: Hemel Hempstead.
34. Mohamed, R. Bayoumi, A.K. (1995 July). Engineering Fracture Mechanics. vol. 51, pp. 861-870.
35. Truong Do, Chang Seop Shin, Dalton Stetsko, Grayson VanConant, Aleksandr Vartanian, Shenli Pei and Patrick Kwon. (2015). Improving Structural Integrity with Boron-Based Additives for 3D printed 420 Stainless Steel. vol. 1, pp. 263-272.
36. Lanzetta, M. and Sachs, E. (2003). Improved surface finish in 3D printing using bimodal powder distribution. Rapid Prototyping Journal. vol. 9, no. 3, pp. 157-166.
37. Window, B. (2006, August 20). Precipitation in copper-iron alloys. pp. 681-699.
38. Deschamps, A, Militzer, M and Poole, W.J. (2001). Precipitation Kinetics and Strengthening of a Fe-0.8wt%Cu Alloy. vol. 41, no. 2, pp. 196-205.
39. Sachs E, Cima, M, and Cornie, J. (2008, January 28). Three-Dimensional Printing: The Physics and Implications of Additive Manufacturing. vol. 42, pp. 257-260.
40. Bogue, R. (2013). 3-D printing: the dawn of a new era in manufacturing? vol. 33, pp. 307-311.
41. Lawrence, E, Martinez, E, Krista, N and Sara, M. (2012, April). Fabrication of Metal and Alloy Components by Additive Manufacturing: Examples of 3D Materials Science. vol. 1, pp. 42-54.
42. Bourell, D, L, Beaman, J. J, Leu, M. C, & Rosen, D. W. (2009). A Brief History of Additive Manufacturing and the 2009 Roadmap for Additive Manufacturing: Looking Back and Looking Ahead. *Proceedings of Rapid Tech 2009. US-TURKEY Workshop on Rapid Technologies*, pp. 1-8, Istanbul.

43. Hickey, Shane. (2014, June 22). Chuck Hull: the father of 3D printing who shaped technology. The Guardian.
44. Sridhara, Reddy, V, Madhava, Ch and Sharath Reddy. (2017, September). 3-D Printing Technologies and Processes. IOSR Journal of Engineering. Vol. 07, pp. 1-14.
45. Sachs E. M, Haggerty, J, S, Cima, M. J. and Williams, P. A. (1993, April 20). Three-dimensional printing techniques. U.S. Patent 5,204,055.
46. Jones, R, Haufe, P, Sells, E, Irvani, P, Olliver, V, Palmer, C. and Bowyer, A. (2011). Robotica. pp. 177–191.
47. http://www.formula1-dictionary.net/rapid_prototyping.html
48. <https://news.nike.com/news/nike-debuts-first-ever-football-cleat-built-using-3d-printing-technology>
49. HRL Laboratories. (2017, September 20). 3D Printing High-Strength Aluminum for Aircraft and Auto Parts.
50. Kyle Wiggers. (2017, April 19). From pixels to plate, food has become 3-D printing's delicious new frontier. Emerging tech, Digital Trends
51. Ferroalloys & Alloying Additives Online Handbook. <http://amg-v.com/copperpage.html>.
52. Copper Development Association Inc. Copper in Iron and Steel P/M Parts. https://www.copper.org/resources/properties/129_6/copper_iron.html.
53. Peng Wen-jie, Xue Huan, Ge Rui and Peng Zhou. (2018). The influential factors on very high cycle fatigue testing results. MATEC Web of Conferences 165, 20002.